Modeling, Parameter Measurement, and Control of PMSG-based Grid-connected Wind Energy Conversion System

Mohammad Kamruzzaman Khan Prince, *Graduate Student Member*, *IEEE*, Mohammad T. Arif, *Member*, *IEEE*, Ameen Gargoom, *Senior Member*, *IEEE*, Aman M. T. Oo, *Senior Member*, *IEEE*, and Md Enamul Haque, *Senior Member*, *IEEE*

***Abstract*—The design of reliable controllers for wind energy conversion systems (WECSs) requires a dynamic model and accurate parameters of the wind generator. In this paper, a dynamic model and the parameter measurement and control of a direct-drive variable-speed WECS with a permanent magnet synchronous generator (PMSG) are presented. An experimental method is developed for measuring the key parameters of the PMSG. The measured parameters are used in the design of the controllers. The generator-side converter is controlled using a vector control scheme that maximizes the power extraction under varying wind speeds. A model predictive controller (MPC) is designed for the grid-side voltage source converter (VSC) to regulate the active and reactive power flows to the power grid by controlling the *d*- and *q*-axis currents in the synchronous reference frame. The MPC predicts the future values of the control variables and takes control actions based on the minimum value of the cost functions. To comply with the grid code requirement, a modified design approach for an LCL filter is presented and incorporated into the system. The design process is simple and incorporates significant filter parameters while avoiding iterative calculations. The comparative analysis of the designed filter with conventional L, LC, and iterative LCL filters demonstrates the effectiveness of the modified design approach. The proposed wind energy system with MPC and LCL filter is simulated in MATLAB/Simulink and experimentally implemented in the laboratory using the dSpace digital signal processor (DSP) system. The simulation and experimental results validate the efficacy of the designed controllers using the measured parameters and show dynamic and steady-state performance under varying wind speeds.**

***Index Terms*—Wind energy, permanent magnet synchronous generator (PMSG), parameter measurement, model predictive controller (MPC), LCL filter.**

I. Introduction

THE popularity of wind energy as a clean and renewable alternative energy source is increasing rapidly [1], [2]. According to the global wind report of Global Wind Energy Council (GWEC) [3], in 2019, the global new-installed wind power surpassed 60 GW, bringing the total installed capacity to 650 GW. The conversion of wind energy and its integration into the power grid depend on the successful implementation of controllers and harmonic filters.

To design an efficient controller for the generator-side converter, a dynamic model of the wind generator (WG) with accurately measured parameters is required. The key parameters include: ① armature resistance; ② permanent magnet flux linkage; and ③ *d*- and *q*-axis inductances. The magnetic saturation and cross-coupling effect affect the measurement accuracy of the *d*- and *q*-axis reactances [4]. The available methods for obtaining the *d*- and *q*-axis reactances include: ① the analytical method; ② the finite-element method (FEM); and ③ experimental tests [5]. The analytical method performs poorly when faced with difficult design challenges owing to the complex flux distribution of the permanent magnet. Some other drawbacks include magnetic saturation and generator structural complexity [4], [5]. In this scenario, the FEM performs better and provides higher measurement accuracy by considering the effects of cross-coupling and magnetic saturation [6]. However, both of the two methods are limited by the dimensions and geometry constraints of the permanent magnet synchronous generator (PMSG). Therefore, the experimental tests are quite significant to measure the PMSG parameters. Additionally, the experimental results can validate the other two methods. Different experimental procedures are available for a salient-pole synchronous machine, but they are not applicable for a surface-mounted PMSG. Feasible experimental methods include the DC bridge, instantaneous flux linkage, vector current-controlled, standstill torque, and AC standstill test methods [4]. Among these methods, the vector current-controlled and AC standstill methods offer higher measurement accuracy.

In field of wind energy, one of the currently most promising system structures is the PMSG-based Type-4 wind energy conversion system (WECS) interfaced to the power grid by a back-to-back two-level voltage source converter (VSC)

Manuscript received: August 13, 2020; accepted: April 22, 2021. Date of CrossCheck: April 22, 2021. Date of online publication: July 14, 2021.

The authors would like to thank Mr. James Lamont, Senior Technical Officer of the Renewable Energy and Electric Vehicle (REEV) Lab, Deakin University, for his constant support during the experiments.

M. K. K. Prince (corresponding author), M. T. Arif, A. Gargroom, A. M. T. Oo, and M. E. Haque are with the Renewable Energy & Electric Vehicle (REEV) Lab, Centre for Smart Power & Energy Research (cSPER), School of Engineering, Deakin University, Waurn ponds, Australia (e-mail: mkprince@deakin.edu.au; m.arif@deakin.edu.au; a.gargoom@deakin.edu.au; aman.m@deakin.edu.au; enamul.haque@deakin.edu.au).

DOI: 10.35833/MPCE.2020.000601

topology. An efficient control strategy for the grid-side converter can ensure the desired system stability and power quality. The existing popular classical control methods include virtual flux-oriented control [7], direct power control [8], and decoupled voltage-oriented control (VOC) [9]-[11]. These controllers employ multiple proportional-integral (PI) regulators that can cause instability owing to the system nonlinearity and the variation of system variables [12], [13]. Moreover, tuning these regulators for suitable gain is a tedious and time-consuming task. To overcome this drawback, the conventional VOC has been replaced by model predictive controller (MPC). In the latter, future events are predicted, and control actions are selected based on the predictions and the minimization of the cost function. The MPC incorporates the nonlinearity of the system plant and offers superior steady-state and dynamic responses to the control variables. Additionally, it has some other advantages such as simplicity, design flexibility, and cost-effectiveness [14].

In a WECS, the nonlinear profiles of the power electronic converters and nonlinear loading result in the harmonic distortion of voltage and current waveforms at the point of common coupling (PCC). Traditionally, the first-order L filter is employed in the grid-connected WECS. Although such filter is simple and easy to design, its drawbacks such as bulkiness, inefficiency, higher voltage drop, and incompatibility with higher switching frequency have led to the design of higher-order alternatives. The third-order LCL filter has become a recent research focus owing to its advantages such as the superior harmonics suppression and reduced size and weight. However, the design process is complex and requires repetitive calculations. The common design guidelines are stated in [15], [16]. The inverter-side inductor and capacitor are sized based on the permissible current ripples due to the switching of inverter and power factor (PF) variations, respectively. The grid-side inductor further eliminates the output current ripples.

The performance of the designed filter must satisfy the existing standards and should not cause resonance within the system control bandwidth [17]. Resonance introduces severe oscillations in the system and makes the overall system unstable. Appropriate damping can reduce the oscillations around the resonant frequency. In this paper, passive damping is preferred over active damping because the latter incorporates additional sensors, high-frequency noises, and complexity into the system. Although passive damping is easy to be implemented, it increases the heat and power losses in the system and decreases the efficiency of the LCL filter. Therefore, the damping resistance should be as small as possible to satisfy other design criteria. Other desirable characteristics include the minimum voltage drop and energy storage, reduced reactive power generation, higher PF operation, lower electromagnetic interference, and robustness to variations in the external system parameters [15], [18], [19]. It is very difficult to achieve all the design goals simultaneously, and most designs consider only certain targets. Researchers select to minimize the power loss [20] and filter capacitance [21], reduce the magnitudes of the filter parameters, increase the robustness against grid impedance variations [16], [22], and reduce the electromagnetic interference [23] as their design targets. However, in the literature mentioned above, the process of determining the resonance frequency requires iterative calculations that are complex and time-consuming.

In this paper, simple experimental techniques are developed to measure the key parameters of the PMSG, and the controller is designed using the measured parameters of the generator-side AC/DC converter. The experimental results verify the effectiveness of the measurement methods. An MPC is also designed for the grid-side DC/AC converter. The effectiveness of the MPC is verified using both simulation and experimental results. The results are further compared with those of a conventional controller. Additionally, a modified method for the design of an LCL filter is proposed to mitigate the harmonic distortion of voltage and current waveforms at the PCC. In this method, the effects of the ratio between the switching frequency and resonant frequency, and that between the grid-side inductance and inverter-side inductance on the harmonic attenuation, filter sizing, and resonance, are analyzed. The analysis gives the necessary tradeoff between minimizing the size of the passive components and the power loss in designing a filter. The presented graphs eliminate the need for iterations and reduce the design complexity. The performance of the designed LCL filter based on the modified design method is compared with conventional L, LC, and iterative LCL filters in terms of frequency response and voltage and current spectrums. The main contributions of this paper are summarized as: ① the development of simple experimental methods to measure the key WG parameters and utilization of the parameters in designing a vector control scheme for a generator-side AC/DC converter; ② the design and experimental validation of an MPC for the grid-side DC/AC converter and the performance comparison with a conventional controller; ③ a modified design of the LCL filter for a grid-connected wind energy system that incorporates significant filter parameters and avoids iterative calculations.

The remainder of this paper is organized as follows. Section II presents the system structure and dynamic modeling of the PMSG and wind turbine. The parameter measurement method is described in Section III. Section IV presents the control schemes for the WECS, followed by the modified design approach of the LCL filter in Section V. Section VI presents the simulation results, the experimental setup and results for the parameter measurement, generator- and grid-side converter controllers, and LCL filter. Finally, the conclusions are presented in Section VII.

II. System Structure and Dynamic Modeling of PMSG and Wind Turbine

Figure 1 shows the structure of the PMSG-based wind energy system with back-to-back VSCs, where MPPT, PI, PWM, and PLL are short for the maximum power point tracking, proportional-integral, pulse-width modulation, and phase-locked loop, respectively. The system under consideration includes a wind turbine, surface magnet-type PMSG, generator- and grid-side converters with associated controllers, DC-link capacitance, LCL filter, coupling transformers, synchronization relays, and the utility grid. The dynamic modeling of the PMSG and wind turbine is presented in the following subsections.

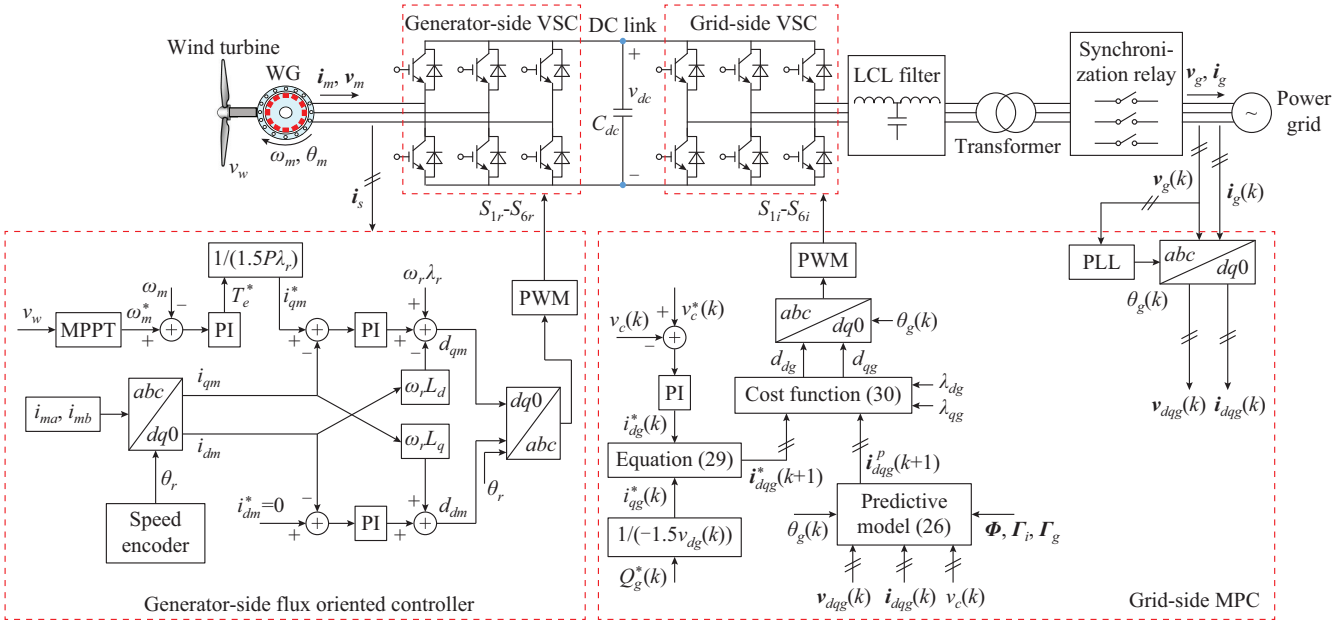

Fig. 1. Schematic diagram of direct-driven PMSG-based wind energy system.

A. Dynamic Modeling of PMSG

The PMSG includes a permanent magnet rather than an excitation winding, which results in a smaller pole pitch and compatibility with low-speed applications. The *d*- and *q*-axis stator voltages, denoted by v_{dm} and v_{qm}, respectively, can be expressed as [24], [25]:

$$v_{dm} = -R_a i_{dm} + \omega_r L_q i_{qm} - L_d p i_{dm} \tag{1}$$

$$v_{qm} = -R_a i_{qm} - \omega_r L_d i_{dm} + \omega_r \lambda_r - L_q p i_{qm} \tag{2}$$

where R_a is the per-phase stator winding resistance; i_{dm} and i_{qm} are the *d*- and *q*-axis stator currents, respectively; ω_r is the speed of *dq* reference frame; L_d and L_q are the *d*- and *q*-axis stator inductances, respectively; λ_r is the rotor flux linkage; and $p = \mathrm{d}/\mathrm{d}t$ is the derivative operator.

L_d and L_q are expressed as:

$$L_d = L_{ls} + L_{dm} \tag{3}$$

$$L_q = L_{ls} + L_{qm} \tag{4}$$

where L_{dm} and L_{qm} are the *d*- and *q*-axis magnetizing inductances, respectively; and L_{ls} is the stator winding leakage inductance. The electromagnetic torque generated from the PMSG (T_e) can be expressed as:

$$T_e = 1.5P[i_{qm}\lambda_r - i_{dm}i_{qm}(L_d - L_q)] \tag{5}$$

where P is the number of pole pairs.

B. Modeling of Wind Turbine

The relationship between the turbine mechanical power P_M and kinetic power of the wind P_w is:

$$P_M = P_w C_p = \frac{1}{2}\rho A_T v_w^3 C_p \tag{6}$$

where C_p is the power coefficient of wind turbine; ρ is the air density; $A_T = \pi r_T^2$ is the turbine blade swept area, r_T is the wind turbine blade length; and v_w is the wind speed. The tip speed ratio (TSR) λ_T of the wind turbine blade should be adjusted based on the variation of the wind speeds to ensure the optimum value of the power coefficient $C_{p,OPT}$ and the extraction of the maximum available wind power. The optimum value of the TSR $\lambda_{T,OPT}$ is defined as:

$$\lambda_{T,OPT} = \frac{\omega_{M,OPT} r_T}{v_w} \tag{7}$$

where $\omega_{M,OPT}$ is the optimum angular speed of the wind turbine.

III. Parameter Measurement of PMSG

In this paper, simple experimental methods are employed to measure the key PMSG parameters. The methods include the DC resistance test, open circuit test, and AC standstill method.

To measure the resistance of PMSG stator winding, a DC power supply is employed to measure the voltage and current of the winding. The resistance R_a is calculated by (8). The value of the resistance changes with temperature variations. To consider the effect of temperature variations, the result from (8) is adjusted using (9).

$$R_a = \frac{V_a}{2I_a} \tag{8}$$

$$R_2 = R_1 + \alpha \Delta T \tag{9}$$

where the resistance R_1 is found at T_1 and changes to R_2 when the temperature changes by $\Delta T = T_2 - T_1$. The temperature coefficient of resistivity takes the value of $\alpha = 0.00393\ ^\circ\mathrm{C}^{-1}$. The machine temperature tends to vary between 45 ℃ and 75 ℃ under actual operating conditions [26]. In this paper, T_2 is assumed to be 60 ℃ (the mean value of the usual operating range).

Assuming a sinusoidal voltage distribution, the phase-to-neutral voltage V_{mln} is given as:

$$V_{mln} = \omega_r \lambda_r \tag{10}$$

$$\omega_r = \frac{2\pi}{60} N_r \frac{P}{2} \tag{11}$$

where N_r is the PMSG rotor speed.

The *d*- and *q*-axis inductances depend on the self- and mutual-inductances of stator winding, which are assumed to be sinusoidally distributed functions of the rotor position θ_r and can be expressed as:

$$L(\theta_r) = L_0 \pm L_2 \cos(2\theta_r) + L_{ls} \tag{12}$$

$$M(\theta_r) = M_0 \pm M_2 \cos\left(2\theta_r \pm \frac{2\pi}{3}\right) \tag{13}$$

where L_0 and M_0 are the DC values of the self- and mutual-inductances, respectively; and L_2 and M_2 are the second harmonic components of the self- and mutual-inductances, respectively. Assuming negligible space harmonics, the mathematical expressions for L_d and L_q are expressed as:

$$L_d = \frac{3}{2}(L_0 - L_2) + L_{ls} \tag{14}$$

$$L_q = \frac{3}{2}(L_0 + L_2) + L_{ls} \tag{15}$$

However, in practice, the space harmonics are quite significant. To account for the space harmonics, (14) and (15) are modified as:

$$L_d = (L_0 - M_0) - \left(\frac{L_2}{2} + M_2\right) + L_{ls} \tag{16}$$

$$L_q = (L_0 - M_0) + \left(\frac{L_2}{2} + M_2\right) + L_{ls} \tag{17}$$

In this paper, the superior AC standstill method is employed to measure the *d*- and *q*-axis inductances, as mentioned in Section I. Figure 2 presents the circuit diagrams for the measurement of *d*- and *q*-axis inductances in cases of PMSG with accessible and inaccessible neutral points. The PMSG employed in the laboratory usually has an inaccessible neutral point.

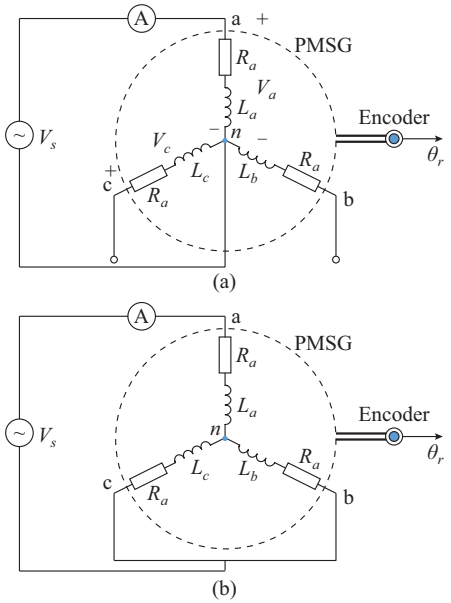

Fig. 2. Measurement of *d*- and *q*-axis inductances. (a) PMSG with accessible neutral point. (b) PMSG with inaccessible neutral point.

Therefore, assuming identical stator windings with similar stator resistances R_a (as shown in Fig. 2(b)), the voltages of three phases V_a, V_b, and V_c are expressed as:

$$V_a = \frac{2}{3} V_s \tag{18}$$

$$V_b = V_c = \frac{1}{3} V_s \tag{19}$$

For the stator winding, the self-inductance of phase a and the mutual-inductance between phases a and c are expressed as:

$$L_a = \frac{\sqrt{\left(\frac{V_a}{I_a}\right)^2 - R_a^2}}{2\pi f_r} \tag{20}$$

$$M_{ac} = \frac{V_c}{2\pi f_r I_a} \tag{21}$$

Although the proposed methods give accurate measurements of the PMSG parameters, they have a few limitations in practice. One limitation is that the neutral point of the PMSG is inaccessible. To overcome this problem, a virtual neutral point is used in this paper. Another limitation is the variation of the stator resistance with temperature, which is eliminated by correcting the measurement for the actual operating conditions.

IV. Control of WECS

The overall control structure of the WECS shown in Fig. 1 includes a generator-side converter controller with the maximum power extraction to regulate the generator speed and capture the maximum power under varying wind speeds, and a grid-side inverter controller to control the active and reactive power flows into the power grid by controlling the *d*- and *q*-axis currents in the synchronously rotating reference frame. The details of these controllers are presented in the following subsections.

A. Control of Generator-side Converter with the Maximum Power Extraction

In this paper, a decoupled current controller is designed for the generator-side VSC, as shown in Fig. 1. According to (6), the TSR must be maintained at $\lambda_{T,OPT}$ to track the maximum available power $P_{M,\max}$ as the wind speed varies. The relationship between P_M and the angular speed of the wind turbine ω_M under varying wind conditions is shown in Fig. 3.

The maximum power points (MPPs) are specified at different wind speeds. To ensure that these points are tracked, the wind turbine should rotate at $\omega_{M,OPT}$. The dynamic equations representing the generator-side converter are expressed as [27]:

$$\begin{cases} L_r p i_{dm} = -R_r i_{dm} + \omega_r L_r i_{qm} - d_{dm} v_{dc} + v_{dm} \\ L_r p i_{qm} = -R_r i_{qm} + \omega_r L_r i_{dm} - d_{qm} v_{dc} + v_{qm} \\ C_{dc} p v_{dc} = d_{dm} i_{dm} + d_{qm} i_{qm} - \dfrac{1}{R_{rl}} v_{dc} \end{cases} \tag{22}$$

where L_r and R_r are the converter input inductance and resistance, respectively; R_{rl} is the equivalent load resistance at

the output terminals; C_{dc} and v_{dc} are the DC-link capacitance and voltage, respectively; and d_{dm} and d_{qm} are the duty cycle ratios for the generator-side converter switches.

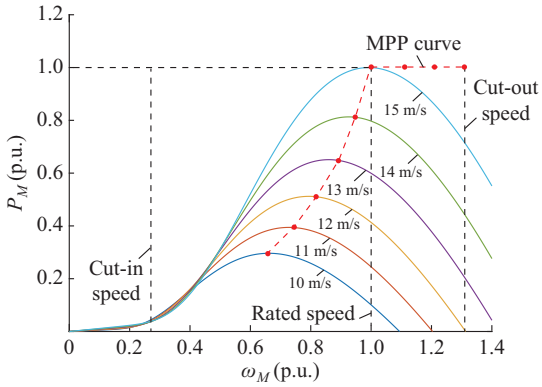

Fig. 3. Relationship between P_M and ω_M.

The values of L_d and L_q are found to be identical in a PMSG [28]. Substituting the values of L_d and L_q in (5), the q-axis current is responsible for the production of the generator torque. The reference torque T_e^* is determined by comparing the reference and measured speeds of the WG. The real-time wind speed v_w is measured using a wind speed sensor (anemometer). Utilizing the measured wind speed v_w and the TSR relationship in (7), the reference WG speed ω_m^* can be computed from (23). The reference and measured speeds of the WG, i.e., ω_m and ω_m^*, are compared. The resultant errors are sent to a PI controller, which in turn determines the required amount of electric torque, i.e., T_e^*.

$$\omega_m^* = \omega_m^* r_{gb} = \frac{\lambda_{T,OPT}}{r_T} v_w = K_1 v_w \tag{23}$$

where r_{gb} is the gear ratio, which is 1 for the direct-driven operation; and $K_1 = \lambda_{T,OPT}/r_T$ can be determined by the rated parameters of the wind turbine. The required amount of q-axis current, i.e., the reference value of q-axis current i_{qm}^*, can be easily determined from (24) by utilizing T_e^*.

$$i_{qm}^* = \frac{T_e^*}{1.5P\lambda_r} \tag{24}$$

As shown in Fig. 1, the d-axis current i_{dm} is kept constant at zero because it does not have any effect on the generation of the reference torque. The benefit of having a zero d-axis current is the minimization of the stator copper loss, which in turn maximizes the efficiency of the WG. The measured d- and q-axis stator currents are compared with their reference values. The resultant errors are sent to the two PI controllers. The PI controller gains are adjusted in such a way that the d- and q-axis generator currents follow the reference values determined by the vector controller. The required gate pulses S_{1r}-S_{6r} for the converter are generated from the PWM block.

B. Control of Grid-side Converter with MPC

In this paper, the MPC regulates three control variables: ① the DC-link voltage; ② the d-axis grid current; and ③ the q-axis grid current. The two-level converter shown in Fig. 1 contains two complementary switches in each converter leg. Therefore, eight different switching pulses and inverter output voltage vectors are available at every switching instant. The discrete time (DT) representation of the inverter output voltage is expressed as [24]:

$$\begin{bmatrix} v_{di}(k) \\ v_{qi}(k) \end{bmatrix} = v_c(k) \begin{bmatrix} S_{di1}(k) \\ S_{qi1}(k) \end{bmatrix} \tag{25}$$

where $v_{di}(k)$ and $v_{qi}(k)$ are the d- and q-axis voltages of the inverter at the k^{th} instant, respectively; $v_c(k)$ is the measured DC-link voltage; and $S_{di1}(k)$ and $S_{qi1}(k)$ are the d- and q-axis switching pulses of the upper leg switch at the k^{th} instant, respectively.

In contrast, the state-space model considering a one-step prediction horizon of the predicted grid currents is expressed as [9]:

$$\begin{bmatrix} i_{dg}^p(k+1) \\ i_{qg}^p(k+1) \end{bmatrix} = \boldsymbol{\Phi} \begin{bmatrix} i_{dg}(k) \\ i_{qg}(k) \end{bmatrix} + \boldsymbol{\Gamma}_i \begin{bmatrix} v_{di}(k) \\ v_{qi}(k) \end{bmatrix} + \boldsymbol{\Gamma}_g \begin{bmatrix} v_{dg}(k) \\ v_{qg}(k) \end{bmatrix} \tag{26}$$

where the superscript p denotes the predicted values; $i_{dg}(k)$ and $i_{qg}(k)$ are the d- and q-axis grid currents, respectively; $v_{dg}(k)$ and $v_{qg}(k)$ are the d- and q-axis grid voltages, respectively; and $\boldsymbol{\Phi}$, $\boldsymbol{\Gamma}_i$, and $\boldsymbol{\Gamma}_g$ are the DT matrices.

The active and reactive power to the power grid (denoted as P_g and Q_g, respectively) are expressed in (27), which are controlled by the d- and q-axis grid currents, respectively.

$$\begin{cases} P_g(k+1) = 1.5 v_{dg}(k) i_{dg}(k+1) \\ Q_g(k+1) = -1.5 v_{dg}(k) i_{qg}(k+1) \end{cases} \tag{27}$$

The structure of the predictive controller is illustrated in Fig. 1. The reference values of the DC-link voltage $v_c^*(k)$ and reactive power $Q_g^*(k)$ are set to be 3.062 p.u. and 0 (unity PF operation), respectively. The reference value of d-axis grid current $i_{dg}^*(k)$ is generated from the outer DC-link voltage control loop, and the reference value of q-axis grid current $i_{qg}^*(k)$ is obtained as:

$$i_{qg}^*(k) = \left. \frac{Q_g^*(k)}{-1.5 v_{dg}(k)} \right|_{v_{qg}(k)=0} \tag{28}$$

The reference values of d- and q-axis grid currents are extrapolated to the $(k+1)^{\text{th}}$ instant by adopting the fourth-order Lagrange extrapolation method as expressed in (29). The errors between the extrapolated and predicted signals are minimized by the cost function as shown in (30).

$$\begin{cases} i_{dg}^*(k+1) = 4i_{dg}^*(k) - 6i_{dg}^*(k-1) + 4i_{dg}^*(k-2) - i_{dg}^*(k-3) \\ i_{qg}^*(k+1) = 4i_{qg}^*(k) - 6i_{qg}^*(k-1) + 4i_{qg}^*(k-2) - i_{qg}^*(k-3) \end{cases} \tag{29}$$

$$g(k) = \lambda_{dg}(i_{dg}^*(k+1) - i_{dg}^p(k+1))^2 + \lambda_{qg}(i_{qg}^*(k+1) - i_{qg}^p(k+1))^2 \tag{30}$$

where λ_{dg} and λ_{qg} are the weighting factors for the d- and q-axis grid currents, respectively.

These factors need to be carefully selected depending on the operating conditions and design requirements. Finally, the switching pulses denoted as S_{1i}-S_{6i} associated with the minimum cost value are generated from the PWM block and applied to the inverter switches.

V. Design of LCL Filter

The per-phase model of the LCL filter is shown in Fig. 4.

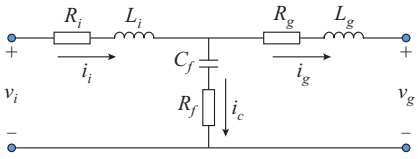

Fig. 4. Per-phase model of LCL filter.

The transfer function of the filter expressed in (31) includes the damping resistance but neglects the resistances associated with the converter- and grid-side inductances.

$$\frac{i_g(s)}{v_i(s)} = \frac{C_f R_f s + 1}{L_i L_g C_f s^3 + L_t C_f R_f s^2 + L_t s} \tag{31}$$

where v_i and i_g are the converter output voltage and grid current, respectively; L_t, L_i, and L_g are the total, converter-side, and grid-side inductances, respectively; and C_f and R_f are the filter capacitance and damping resistance, respectively. The mathematical expression for the filter resonance frequency f_{res} is shown in (32). Some simple mathematical manipulations of (32) lead to the expression as shown in (33).

$$f_{res} = \sqrt{\frac{L_t}{4\pi^2 L_i L_g C_f}} \tag{32}$$

$$L_t C_f = \frac{[r_f(1+r_L)]^2}{\omega_{sw}^2 r_L} \tag{33}$$

where $r_f = f_{sw}/f_{res}$ is the ratio between the switching frequency f_{sw} and resonance frequency f_{res}; and $r_L = L_g/L_i$ is the ratio between the grid-side inductance L_g and converter-side inductance L_i. These ratios must be selected properly to ensure an efficient design of LCL filter. A suitable selection of the ratios can avoid the need for iterative calculations.

According to the Nyquist sampling criteria, the resonance frequency must be lower than half of the sampling frequency f_s so that the resonance is visible to the digital signal processor (DSP). However, the resonance should not occur within the system control bandwidth f_{bw}. Therefore, the resonance range can be set as [18]:

$$f_{bw} < f_{res} < f_s/2 \tag{34}$$

Considering double-update PWM ($f_s = 2f_{sw}$) for the digital implementation of the controller and substituting $f_{bw} \approx f_s/(6\pi)$ [29], (34) can be rewritten as:

$$1 < r_f < 9.43 \tag{35}$$

Any value of r_f within the range specified by (35) can be used, but the resultant filter must comply with other design criteria such as small sizes of the passive components, reduced power loss, total harmonic distortion (THD), reactive power generation and PF variations, and improved robustness.

As mentioned in Section I, the modified design approach of filter proposed in this paper implements a passive damping scheme. The required amount of damping can be determined using (36). The critical frequency $f_c = f_s/6$ separates the damping regions [30]. Assuming $f_c = f_{res}$, the ratio r_f is found to be 3. The system is unstable at $r_f = 3$ owing to a pair of open-loop unstable poles. Therefore, $r_f = 3$ is avoided in the modified design.

$$R_f = \frac{1}{3\omega_{res} C_f} \tag{36}$$

The mathematical expressions of the base impedance Z_b, capacitance C_b, and inductance L_b are shown in (37)-(39), respectively.

$$Z_b = \frac{V_{gll}^2}{P_g} \tag{37}$$

$$C_b = \frac{1}{\omega_g Z_b} \tag{38}$$

$$L_b = \frac{Z_b}{2\pi f_g} \tag{39}$$

where V_{gll} and f_g are the line-to-line voltage and line frequency of the grid, respectively. Formula (40) is derived from (31) by setting $s = h = \mathrm{j}\omega_{sw}$ ($\omega_{sw} = 2\pi f_{sw}$), which represents the minimum value of the total inductance $L_{t,\min}$. The damping term is neglected in (40).

$$L_{t,\min} = \frac{1}{\omega_{sw} \left| i_g(h)/v_i(h) \right| \left| 1 - r_f^2 \right|} \tag{40}$$

where $\left| i_g(h)/v_i(h) \right|$ denotes the attenuation coefficient of the grid-side current magnitude. The current harmonic limits in Table I are specified by the IEEE-519 standards [17]. In Table I, *TDD* denotes the total demand distortion. The individual odd harmonics are represented by h which are specified for $I_{sc}/I_L < 20$. Here, I_{sc}/I_L represents the ratio between the maximum short-circuit current at the PCC and maximum demand load current at the PCC under normal load operating conditions.

TABLE I
Current Harmonic Limits

Limits					*TDD*
$3 \le h < 11$	$11 \le h < 17$	$17 \le h < 23$	$23 \le h < 35$	$35 \le h$	
4.0	2.0	1.5	0.6	0.3	5.0

The maximum capacitance is found by substituting $L_{t,\min}$ into (33), which in turn determines the maximum PF variation α:

$$C_f = \alpha C_b \tag{41}$$

The total inductance L_t must be greater than or equal to the minimum inductance, i.e., $L_t \ge L_{t,\min}$. The converter- and grid-side inductances can be calculated by (42) and (43), respectively.

$$L_i = \frac{L_t}{1 + r_L} \tag{42}$$

$$L_g = \frac{r_L L_t}{1 + r_L} \tag{43}$$

VI. Results and Analysis

The WECS shown in Fig. 1 is implemented in MATLAB/Simulink environment. Rigorous simulation studies have been carried out under various operating conditions to demonstrate the effectiveness of the designed controllers with the measured generator parameters. The system parameters for the PMSG, wind turbine, utility grid, and filters are listed in Tables II-IV. In the simulation model, a detailed model is considered for the back-to-back VSCs. Simulations have been performed to validate the performance of the generator-side converter controllers with the maximum power extraction, grid-side converter controllers with active and reactive power regulation, and LCL filter with the mitigation of high-frequency switching harmonics of the inverter output voltage and current. Table IV lists the parameters for the L, LC, iterative LCL, and modified LCL filters. The sampling time used for the simulation studies is 25 μs and 125 μs for the inner and outer control loops, respectively. Additionally, a reduced-scale experimental setup has been developed in the laboratory to validate the designed controller and LCL filter. In the following subsections, the simulation results, experimental setup, and results are presented in detail.

TABLE II
Measured Parameters for PMSG

Parameter	Value
Stator resistance R_a (DC)	1.28 Ω
Stator resistance R_a (AC)	1.43 Ω
Rotor flux linkage λ_r	0.26 Wb
d- and q-axis inductances $L_d = L_q$	42.76 mH

TABLE III
Parameters for PMSG and Wind Turbine

Parameter	Value
Rated power P_m	2.5 kW
Rated voltage V_{mll}	281 V
Rated current I_m	5.14 A
Rated speed n_m	1500 rad/min
Rated torque T_m	16 N·m
Pole pairs P_p	4
Moment of inertia (without brake)	14.2 kg·cm^2
Mass (without brake)	15.5 kg
Radius of wind turbine blade	0.91 m
Rated wind speed	15 m/s

A. Simulation Results

1) Performance of Generator-side Flux Oriented Controller

The main objective of the generator-side VSC controller is to extract the maximum power from intermittent wind while keeping the PMSG stator loss being the minimum. Figure 5 shows the performance of the generator-side PWM converter controller under varying wind speeds. The variations of the wind speed are presented in Fig. 5(a), whereas Fig. 5(b) shows that the WG speed follows the reference speed under varying wind conditions.

TABLE IV
Parameters of Grid and Filter

Type	Parameter	Value
Grid	Rated power S_g	2.5 kVA
	Rated voltage V_{gll}	281 V
	Rated current I_g	5.14 A
	Rated frequency f_g	50 Hz
	DC-link reference voltage v_{dc}^*	496.76 V (3.062 p.u.)
	Sampling time T_s	25 μs
Modified LCL filter	Switching frequency f_{sw}	20 kHz
	Converter-side inductance L_i	2.1226 mH
	Grid-side inductance L_g	2.1226 mH
	Filter capacitance C_f	0.9547 μF
	Damping resistance R_f	11.114 Ω
Iterative LCL filter	Converter-side inductance L_i	5.6583 mH
	Grid-side inductance L_g	0.3743 mH
	Filter capacitance C_f	1.015 μF
	Damping resistance R_f	6.1995 Ω
LC filter	Filter inductance L	2.117 mH
	Filter capacitance C	3.3145 μF
	Damping resistance R_f	25.273 Ω
L filter	Filter inductance L	19.96 mH (0.2 p.u.)
	Filter resistance R	0.3136 Ω (0.01 p.u.)

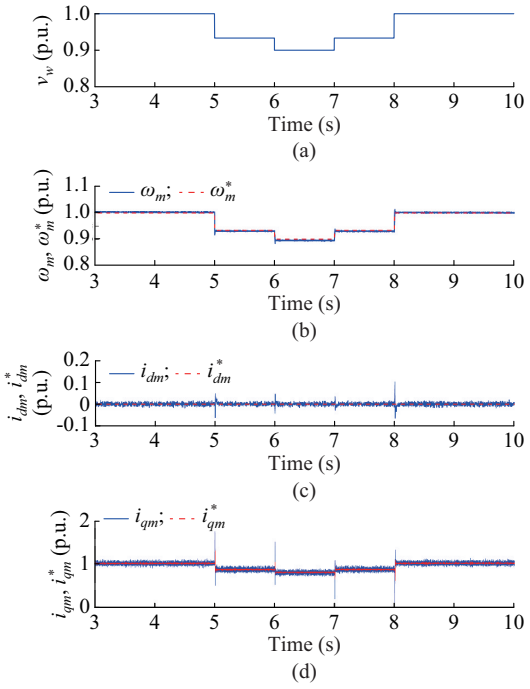

Fig. 5. Performance of generator-side converter controller. (a) Variation of wind speeds. (b) WG speed. (c) d-axis current. (d) q-axis current.

The PMSG rotates at the optimum speed calculated by the MPPT algorithm, which ensures the extraction of the maximum wind power under variable wind speeds. Figure 5(c) and (d) shows the d- and q-axis stator currents, along with their respective reference values. It can be observed that the current controllers can regulate the d- and q-axis currents ef-

fectively under both steady-state and dynamic conditions. The control of the *d*-axis current ensures that the stator loss is minimized while the optimum generator torque is produced by the *q*-axis current. The input and output torque and power of PMSG are shown in Fig. 6. The torque and power of the turbine and generator vary with the change under the wind conditions. The wind speed variation occurs at 5, 6, 7, and 8 s. For example, at 8 s, the wind speed returns to the base value, and the MPPT controller, generator torque, and power responded with the corresponding rated values. From Fig. 6, the generator produces the rated torque and power at the base wind speed of 15 m/s.

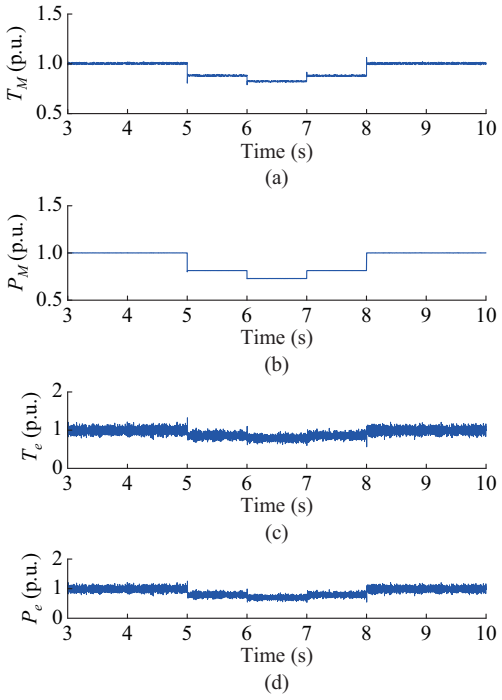

Fig. 6. Input and output torque and power of PMSG. (a) T_M. (b) P_M. (c) T_e. (d) P_M.

2) Performance of Grid-side MPC

The functions of the grid-side MPC are to regulate the DC-link voltage and the *d*- and *q*-axis grid currents to control the active and reactive power flowing into the power grid. Figure 7 shows the DC-link voltage, grid currents, and power flowing into the power grid. Figure 7(a) shows the performance of the outer DC-link voltage control loop, which generates the reference values of the *d*-axis grid current. In Fig. 7(b), the measured *d*-axis grid current tightly follows reference value to regulate the active power flow. Figure 7(c) shows the *q*-axis grid current, which closely follows its reference value to regulate the reactive power flow. i_{qg}^* is set to be zero in order to achieve unity PF operation without reactive power flow. The active power and reactive power flowing into the grid are shown in Fig. 7(d) and (e), respectively. The wind speed variation is reflected by the power flows at 5, 6, 7, and 8 s.

In addition to the MPC, the performance of the conventional VOC is presented in Fig. 8. It is apparent from Figs. 7 and 8 that the MPC offers much better regulation of the control variables in terms of the steady state and transient responses.

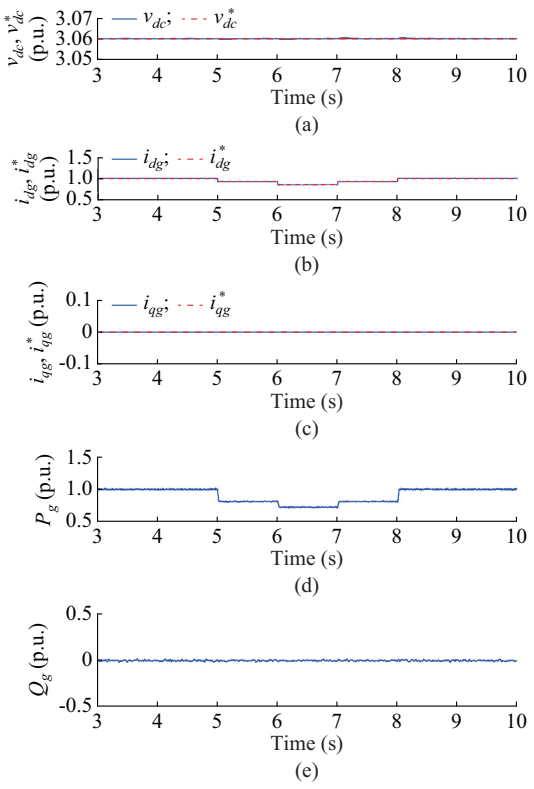

Fig. 7. Performance of grid-side MPC. (a) DC-link voltage. (b) *d*-axis grid current. (c) *q*-axis grid current. (d) Active power flow. (e) Reactive power flow.

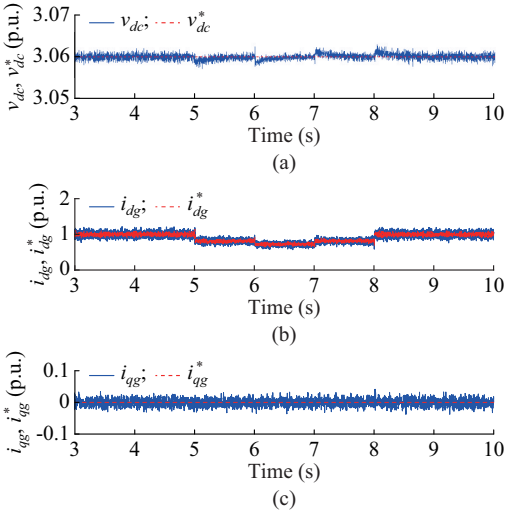

Fig. 8. Performance of conventional VOC. (a) DC-link voltage. (b) *d*-axis grid current. (c) *q*-axis grid current.

3) Performance of Modified LCL Filter

As mentioned in Section V, the design of the modified LCL filter described in this paper accounts for the significance of ratios such as r_L and r_f. Figure 9 shows the minimum values of $L_t C$ when $r_L = 1$. The variations of the damping resistor R_f, heat loss $P_{loss} = I^2 R$, total inductance L_t, and *THD* within the selected range of r_f are shown in Fig. 10. The minimum PF variation is considered in the graphs. As shown in Fig. 10, the minimum sizing of the passive ele-

ments and power loss can be achieved for r_f between 3 to 5. Although *THD* is increased within the selected range of r_f, it is still well below the standards specified by IEEE-519 standards. Allowing higher PF variations further reduces the size of the passive elements at the expense of higher reactive power generation and *THD*. In this paper, the LCL filter is designed for $r_f=4$ and the corresponding filter parameters are listed in Table IV.

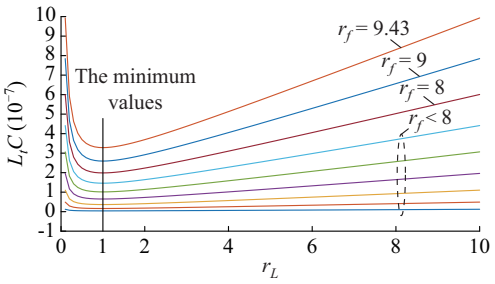

Fig. 9. Significance of r_L and r_f on passive elements sizing.

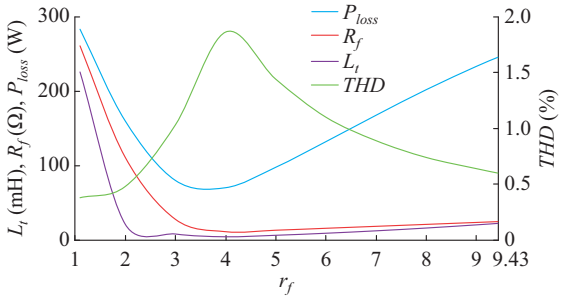

Fig. 10. Variations of damping resistor, power loss, total inductance, and *THD*.

To compare the filter performance, L, LC, and iterative LCL filters are designed with identical system parameters. The corresponding filter parameters are presented in Table IV. The frequency responses, voltage, and current waveforms at the PCC, and harmonic spectra are compared in Figs. 11-13, respectively, among the L, LC, iterative LCL, and modified LCL filters. It is clear from Fig. 11 that the damping smoothens out the gain spike at the resonant frequency, which is represented by the dotted lines. The L filter has a 20 dB/decade attenuation over the full frequency range. In comparison, the LC and LCL filters have 12 dB/octave and 60 dB/decade attenuation, respectively, after the cut-off frequency. The modified design has a lower resonance frequency than the iterative approach. According to (33), a lower resonance frequency facilitates a smaller size of the filter parameters. Figure 12 shows one cycle of the voltage and current waveforms at the PCC for the designed L, LC, iterative LCL, and modified LCL filters. The respective *THD* values are listed in Table V and satisfy the IEEE requirement of less than 5% *THD* for all designs. However, comparing the filter parameters listed in Table IV, the sizes of the passive components of the L and LC filters are larger than those of the LCL filter. The odd harmonics in the voltage and current waveforms at the PCC are compared in Fig. 13(a) and (b), respectively, for the four types of filters. It can be concluded from Figs. 11-13 and Table V that the modified LCL filter offers better performance and smaller size than the conventional filters.

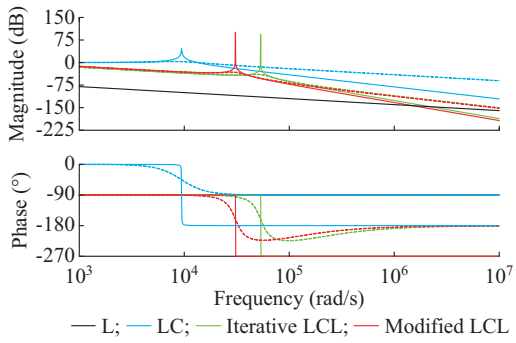

Fig. 11. Comparison of frequency responses.

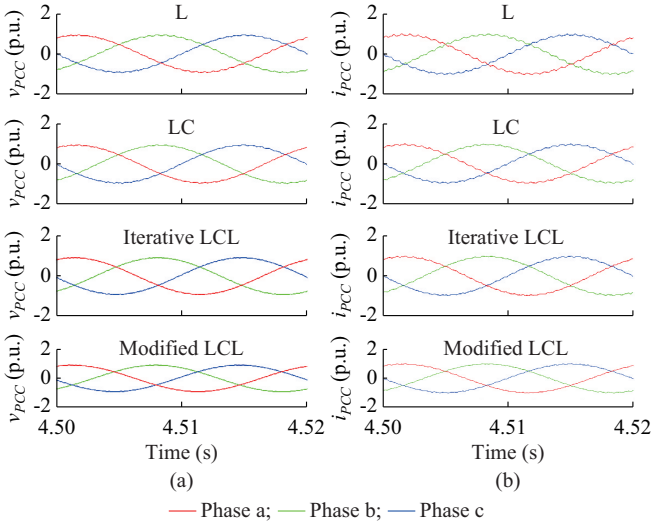

Fig. 12. Comparison of voltage and current waveforms at PCC. (a) Voltage. (b) Current.

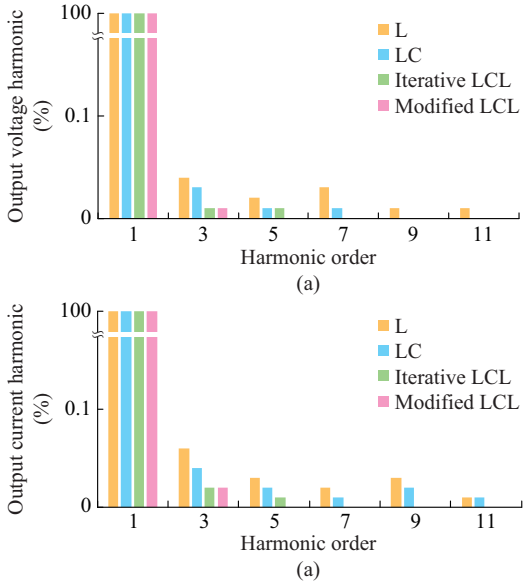

Fig. 13. Odd harmonics in voltage and current waveforms at PCC. (a) Voltage. (b) Current.

TABLE V
COMPARISON OF *THD* LEVEL

Filter type	*THD* of v_{PCC} (%)	*THD* of i_{PCC} (%)
L	2.51	3.60
LC	1.62	2.77
Iterative LCL	0.99	2.03
Modified LCL	0.89	1.86

Moreover, the modified design shows a slightly better ability of harmonic suppression than the iterative one, although the main advantage of the modified design is the avoidance of repetitive calculations. The significance of the ratios r_L and r_f is incorporated into the design, and the resonance frequency is specified prior to the design of the filter passive elements.

B. Experimental Setup

The experimental setup for the PMSG parameter measurement is shown in Appendix A Fig. A1. A reduced-scale 0.64 kW wind energy system has been developed in the laboratory using dSpace Microlabbox DSP system. An induction motor simulates the wind turbine operation and drives the WG at different rotor speeds, as shown in Appendix A Fig. A1(a). Figure A1(b) shows the schematic diagram of the three-phase stator winding, which is wye connected. A DC power supply is connected between phases a and b, whereas phase c is left open. The controllers are designed and implemented using the measured parameters listed in Table II and the dynamic model of the generator shown in Section II-A. A sampling time of 100 μs is used for the implementation of the controllers.

C. Experimental Results

The parameters measured for the PMSG are listed in Table II. Similar experimental approaches are applicable to large WGs. The voltage across and current through the windings are measured using a voltmeter and ammeter, respectively. Initially, the DC resistance is measured to be 1.113 Ω measured at 19 ℃. The resultant DC stator resistance is found to be 1.28 Ω considering the effect of temperature variations. An AC resistance of 1.43 Ω is measured for the 50 Hz AC supply, taking skin effects into consideration.

To measure the WG flux linkage, the rotor speed N_r and phase-to-phase voltages V_{mll} are measured. At the rated frequency of 50 Hz, the value of the flux linkage is measured to be 0.256 Wb. Figure 14 shows the variation of the open-circuit voltage with the generator speed. The open-circuit voltage varies linearly at lower speeds and saturates at higher speeds. The measured values of the flux linkage are plotted with respect to the corresponding generator speeds and phase voltages, which are shown in Fig. 15(a) and (b), respectively. The values of the flux linkage are both found to be 0.256 Wb.

Figure 16 shows the variation of the self- and mutual-inductances with the rotor position within the range of 0° to 360°. The self- and mutual-inductances can be expressed in (12) and (13), respectively.

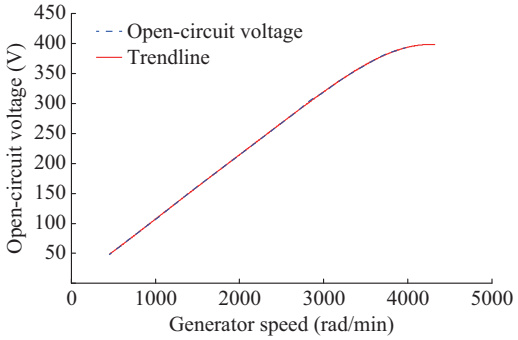

Fig. 14. Open-circuit voltage of WG.

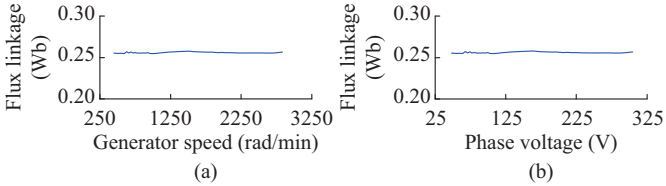

Fig. 15. Measured value of flux linkage with generator speed and phase voltage. (a) Generator speed. (b) Phase voltage.

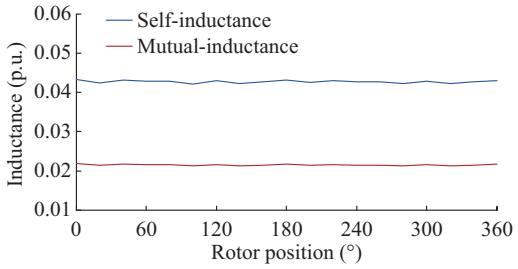

Fig. 16. Variation of self- and mutual-inductances with rotor positions.

The DC terms and second harmonic components can be determined using these mathematical expressions. The least-squares curve-fitting tool has been employed to determine the values of L_0, M_0, L_2, and M_2. Finally, the L_d and L_q have been calculated from (14) - (17). The inductance values are comparable. As shown in Fig. 16, the maxima and minima of the self-inductance curve differ by a very small margin. This small variation is caused by the small saliency in the PMSG employed in this paper. Therefore, the *d*- and *q*-axis inductances are measured as 42.76 mH, i. e., $L_d = L_q =$ 42.76 mH.

Figures 17 and 18 represent the performances of grid-side converter and filter. The *d*- and *q*-axis grid currents with their corresponding reference values are shown in Fig. 17. The voltage and current waveforms at the PCC are presented in Fig. 18. The instantaneous waveforms at the PCC are captured by the MDO 3024 mixed domain oscilloscope. The corresponding *THD* - *F* (fundamental harmonic component) and *THD* - *R* (root mean square harmonic component) values are listed in Table VI. The harmonic analysis shows the *THD* - *F* values of 2.05% and 3.75% for the voltage and current waveforms, respectively, which comply with the IEEE standard of having less than 5% harmonic distortions at the PCC.

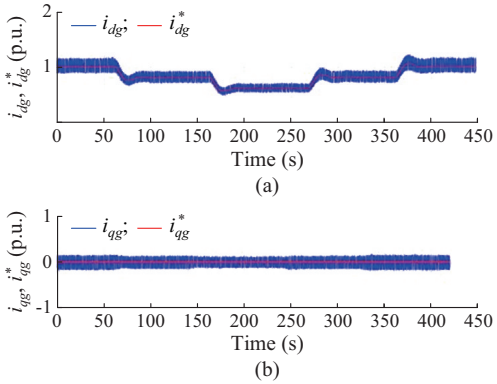

Fig. 17. Experimental results for grid-side converter controller. (a) *d*-axis current. (b) *q*-axis current.

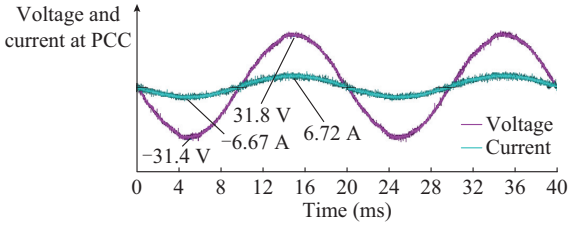

Fig. 18. Experimental verification of LCL filter performance.

TABLE VI
THD VALUES AT PCC

Waveform	*THD* - *F* (%)	*THD* - *R* (%)
Voltage	2.05	2.05
Current	3.75	3.71

VII. CONCLUSION

In this paper, simple experimental methods for the measurement of key PMSG parameters are presented and then used to design controllers for a back-to-back VSC in a direct-driven PMSG-based wind energy system. The simulation and experimental results at different stages of the power conversion demonstrate the effectiveness of the designed controllers. The controllers facilitate the extraction of the maximum available wind power and the regulation of active/reactive power flow to the power grid under varying wind speed conditions. The grid-side MPC successfully predicts the control variables and select control actions based on the minimum cost function values. The presented results demonstrate the superior steady-state and dynamic performances of the predictive controller compared with the conventional one. On the other hand, a modified design approach for an LCL filter is presented in this paper. The design approach incorporates the significance of the important parameters and avoids iterative calculations. The performance of the designed filter is compared with conventional L and LC filters and an iteratively designed LCL filter. Based on the simulation and experimental results, it can be concluded that the modified design approach is a simple, cost-effective, and efficient alternative to existing methods.

APPENDIX A

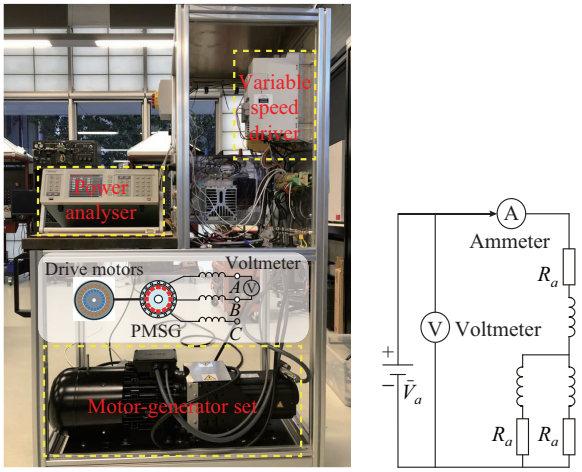

Fig. A1. Experimental setup. (a) Flux linkage measurement. (b) DC resistance test for the measurement of R_a.

REFERENCES

[1] V. Yaramasu, A. Dekka, M. J. Durán *et al*., "PMSG-based wind energy conversion systems: survey on power converters and controls," *IET Electric Power Applications*, vol. 11, no. 6, pp. 956-968, Jul. 2017.
[2] A. Aziz, A. M. T. Oo, and A. Stojcevski, "Issues and mitigations of wind energy penetrated network: Australian network case study," *Journal of Modern Power Systems and Clean Energy*, vol. 6, no. 6, pp. 1141-1157, Nov. 2018.
[3] J. Lee and F. Zhao.(2020, Mar.). Global wind report 2019. [Online]. Available: https://gwec.net/global-wind-report-2019/
[4] R. Dutta and M. F. Rahman, "A comparative analysis of two test methods of measuring *d*- and *q*-axes inductances of interior permanent-magnet machine," *IEEE Transactions on Magnetics*, vol. 42, no. 11, pp. 3712-3718, Nov. 2006.
[5] J. F. Gieras, E. Santini, and M. Wing, "Calculation of synchronous reactances of small permanent-magnet alternating-current motors: comparison of analytical approach and finite element method with measurements," *IEEE Transactions on Magnetics*, vol. 34, no. 5, pp. 3712-3720, Sept. 1998.
[6] M. M. Chowdhury, M. E. Haque, D. Das *et al*., "Modeling, parameter measurement and sensorless speed estimation of IPM synchronous generator for direct drive variable speed wind turbine application," *International Transaction on Electrical Energy Systems*, vol. 25, no. 9, pp. 1814-1830, Apr. 2014.
[7] J. A. Suul, A. Luna, P. Rodríguez *et al*., "Virtual-flux-based voltage-sensor-less power control for unbalanced grid conditions," *IEEE Transactions on Power Electronics*, vol. 27, no. 9, pp. 4071-4087, Sept. 2012.
[8] J. Hu and Z. Q. Zhu, "Investigation on switching patterns of direct power control strategies for grid-connected DC-AC converters based on power variation rates," *IEEE Transactions on Power Electronics*, vol. 26, no. 12, pp. 3582-3598, Dec. 2011.
[9] R. Teodorescu, M. Liserre, and P. Rodriguez, *Grid Converters for Photovoltaic and Wind Power Systems*. Chichester: Wiley-IEEE Press, 2011.
[10] V. Yaramasu, B. Wu, and J. Chen, "Model-predictive control of grid-tied four-level diode-clamped inverters for high-power wind energy conversion systems," *IEEE Transactions on Power Electronics*, vol. 29, no. 6, pp. 2861-2873, Jun. 2014.
[11] M. M. Chowdhury, M. E. Haque, S. Saha *et al*., "An enhanced control scheme for an IPM synchronous generator based wind turbine with MTPA trajectory and maximum power extraction," *IEEE Transactions on Energy Conversion*, vol. 33, no. 2, pp. 556-566, Jun. 2018.
[12] M. A. Soliman, H. M. Hasanien, A. Al-Durra *et al*., "High performance frequency converter controlled variable-speed wind generator using linear-quadratic regulator controller," *IEEE Transactions on Industry Applications*, vol. 56, no. 5, pp. 5489-5498, Sept.-Oct. 2020.
[13] M. A. Soliman, H. M. Hasanien, A. Al-Durra *et al*., "A novel adaptive

control method for performance enhancement of grid-connected variable-speed wind generators," *IEEE Access*, vol. 8, pp. 82617-82629, May 2020.
[14] N. F. Silva, C. E. T. Dórea, and A. L. Maitelli, "An iterative model predictive control algorithm for constrained nonlinear systems," *Asian Journal of Control*, vol. 21, no. 5, pp. 2193-2207, Sept. 2019.
[15] M. Liserre, F. Blaabjerg, and A. Dell'Aquila, "Step-by-step design procedure for a grid-connected three-phase PWM voltage source converter," *International Journal of Electronics*, vol. 91, pp. 445-460, Feb. 2007.
[16] A. Reznik, M. G. Simões, A. Al-Durra *et al*., "LCL filter design and performance analysis for grid-interconnected systems," *IEEE Transactions on Industry Applications*, vol. 50, no. 2, pp. 1225-1232, Mar.-Apr. 2014.
[17] *IEEE Recommended Practice and Requirements for Harmonic Control in Electric Power Systems*, IEEE Standard 519-2014, 2014.
[18] R. Peña-Alzola, M. Liserre, F. Blaabjerg *et al*., "LCL-filter design for robust active damping in grid-connected converters," *IEEE Transactions on Industrial Informatics*, vol. 10, no. 4, pp. 2192-2203, Nov. 2014.
[19] S. Jayalath and M. Hanif, "Generalized LCL-filter design algorithm for grid-connected voltage-source inverter," *IEEE Transactions on Industrial Electronics*, vol. 64, no. 3, pp. 1905-1915, Mar. 2017.
[20] P. Channegowda and V. John, "Filter optimization for grid interactive voltage source inverters," *IEEE Transactions on Industrial Electronics*, vol. 57, no. 12, pp. 4106-4114, Dec. 2010.
[21] A. Kouchaki and M. Nymand, "Analytical design of passive LCL filter for three-phase two-level power factor correction rectifiers," *IEEE Transactions on Power Electronics*, vol. 33, no. 4, pp. 3012-3022, Apr. 2018.
[22] Y. Tang, W. Yao, P. C. Loh *et al*., "Design of LCL-filters with LCL resonance frequencies beyond the Nyquist frequency for grid-connected inverters," in *Proceedings of 2015 IEEE Energy Conversion Congress and Exposition (ECCE)*, Montreal, Canada, Jul. 2015, pp. 5137-5144.
[23] Y. Liu and C.-M. Lai, "LCL filter design with EMI noise consideration for grid-connected inverter," *Energies*, vol. 11, no. 7, pp. 1646-1655, Jun. 2018.
[24] V. Yaramasu and B. Wu, *Model Predictive Control of Wind Energy Conversion Systems*. New Jersey: John Wiley & Sons, 2016.
[25] F. Bakhtiari and J. Nazarzadeh, "Optimal estimation and tracking control for variable-speed wind turbine with PMSG," *Journal of Modern Power Systems and Clean Energy*, vol. 8, no. 1, pp. 159-167, Jan. 2020.
[26] T. Kalogiannis, E. Malz, E. M. Llano *et al*., "Alternative parameter determination methods for a PMSG," in *Proceedings of 2014 International Conference on Optimization of Electrical and Electronic Equipment (OPTIM)*, Bran, Romania, May 2014, pp. 483-488.
[27] R. Gao, X. She, I. Husain *et al*., "Solid-state-transformer-interfaced permanent magnet wind turbine distributed generation system with power management functions," *IEEE Transactions on Industry Applications*, vol. 53, no. 4, pp. 3849-3861, Jul.-Aug. 2017.
[28] M. K. K. Prince, M. E. Haque, M. T. Arif *et al*., "Parameter measurement and modelling of PMSG based wind turbine," in *Proceedings of 2019 29th Australasian Universities Power Engineering Conference (AUPEC)*, Nadi, Fiji, Nov. 2019, pp. 1-6.
[29] V. Blasko and V. Kaura, "A novel control to actively damp resonance in input LC filter of a three-phase voltage source converter," *IEEE Transactions on Industry Applications*, vol. 33, no. 2, pp. 542-550, Mar.-Apr. 1997.
[30] S. G. Parker, B. P. McGrath, and D. G. Holmes, "Regions of active damping control for LCL filters," *IEEE Transactions on Industry Applications*, vol. 50, no. 1, pp. 424-432, Jan.-Feb. 2014.

Mohammad Kamruzzaman Khan Prince received the B.Sc. degree in electrical and electronic engineering from Rajshahi University of Engineering and Technology, Rajshahi, Bangladesh, in 2012. He has been working as an Assistant Professor in the Department of Electrical and Electronic Engineering at Shahjalal University of Science and Technology, Sylhet, Bangladesh, since 2017. He is currently pursuing the Ph.D. degree in the School of Engineering at Deakin University, Waurn Ponds, Australia. His research interests include design of power electronic converters, controllers, energy storage system and stability analysis for integration of renewable energy sources in power system, and electric vehicle (EV).

Mohammad T. Arif received the Bachelor's degree in electrical engineering from University of Engineering & Technology (UET), Lahore, Pakistan, in 1999, the Master's degree in media communication engineering from Hanyang University, Seoul, South Korea, in 2006, and the Ph.D. degree in electrical engineering from Central Queensland University, Queensland, Australia, in 2013, respectively. He is currently working as a Lecturer at Deakin University, Waurn Ponds, Australia. His research interests include renewable energy, energy storage, electric vehicle and their impact assessment & integration into power grid, energy efficiency, energy management and power system protection for grid and microgrid applications.

Ameen Gargoom received the B.Sc. and M.Sc. degrees in electrical and electronic engineering from Benghazi University, Benghazi, Libya, and the Ph.D. degree in electrical engineering from The University of Adelaide, Adelaide, Australia, in 1995, 2002, and 2008, respectively. He is currently a Lecturer at Deakin University, Geelong, Australia. His research interests include renewable energy integration and energy storage systems in power systems.

Aman M. T. Oo received the Master's and Ph.D. degrees in electrical engineering from the University of Melbourne, Melbourne, Australia and Victoria University, Melbourne, Australia, respectively. He is currently the Dean and Head of School of Engineering at Deakin University, Waurn Ponds, Australia. He is a Professor of electrical engineering and has made significant research contributions in the area of electrical power engineering and renewable energy, engineering education. His research interests include microgrid & energy storage system integration, smart grid communication, power system stability and control, energy management and efficiency, protection and security of smart grids, sustainable operation and control of microgrids as well as in engineering education.

Md Enamul Haque received the B.Sc. degree in electrical and electronic engineering from Bangladesh Institute of Technology (BIT), Rajshahi, Bangladesh, in 1995, the M.Eng. degree in electrical engineering from University Technology Malaysia (UTM), Kuala Lumpur, Malaysia, in 1998, and the Ph.D. degree in electrical engineering from University of New South Wales (UNSW), Sydney, Australia, in 2003. He is currently working as a Senior Lecturer in the School of Engineering, Deakin University, Waurn Ponds, Australia. His research interests include control of power electronic converters for renewable energy systems, battery/supercapacitor energy storage system, electric vehicle, motor drives, microgrid and cyber security in microgrid/smart grid.